ARL-TR-9017 ● AUG 2020

DEVCOM ARMY RESEARCH LABORATORY

Roll Orientation–Dependent Aerodynamics of a Long-Range Projectile

by Joseph D Vasile and Jubaraj Sahu

NOTICES

Disclaimers

The findings in this report are not to be construed as an official Department of the Army position unless so designated by other authorized documents.

Citation of manufacturer's or trade names does not constitute an official endorsement or approval of the use thereof.

Destroy this report when it is no longer needed. Do not return it to the originator.

ARL-TR-9017 ● AUG 2020

Roll Orientation–Dependent Aerodynamics of a Long-Range Projectile

Joseph D Vasile
Weapons and Materials Research Directorate, CCDC Army Research Laboratory

Jubaraj Sahu
Oak Ridge Associated Universities

REPORT DOCUMENTATION PAGE

Form Approved
OMB No. 0704-0188

1. REPORT DATE *(DD-MM-YYYY)*	2. REPORT TYPE	3. DATES COVERED
August 2020	Technical Report	1 December 2019–1 April 2020

4. TITLE AND SUBTITLE
Roll Orientation–Dependent Aerodynamics of a Long-Range Projectile

5a. CONTRACT NUMBER

5b. GRANT NUMBER

5c. PROGRAM ELEMENT NUMBER

6. AUTHOR(S)
Joseph D Vasile and Jubaraj Sahu

5d. PROJECT NUMBER

5e. TASK NUMBER

5f. WORK UNIT NUMBER

7. PERFORMING ORGANIZATION NAME(S) AND ADDRESS(ES)
CCDC Army Research Laboratory
ATTN: FCDD-RLW-LE
Aberdeen Proving Ground, MD 21005

8. PERFORMING ORGANIZATION REPORT NUMBER
ARL-TR-9017

9. SPONSORING/MONITORING AGENCY NAME(S) AND ADDRESS(ES)

10. SPONSOR/MONITOR'S ACRONYM(S)

11. SPONSOR/MONITOR'S REPORT NUMBER(S)

12. DISTRIBUTION/AVAILABILITY STATEMENT
Approved for public release; distribution is unlimited.

13. SUPPLEMENTARY NOTES
ORCID ID(s): Joseph D Vasile, 0000-0003-3812-6277; Jubaraj Sahu, 0000-0003-3347-4387

14. ABSTRACT
A computational investigation was performed to determine the aerodynamic coefficient's dependence on roll orientation for a low-aspect-ratio finned projectile. Navier–Stokes (CFD++) and inviscid (Cart3D) computational fluid dynamics flow solvers were used to characterize the aerodynamics of the flight vehicle. The results suggest that viscous flow phenomena become relevant when the lifting fins are oriented leeward on the projectile at moderate to high angles of attack. To improve our understanding of the flow physics associated with the observed phenomena, the generation and advection of the vortical flow structures produced by the fins were studied.

15. SUBJECT TERMS
long-range guided projectiles, computational fluid dynamics, aerodynamic characterization, roll-orientation dependence, roll-orientation aerodynamics

16. SECURITY CLASSIFICATION OF:			17. LIMITATION OF ABSTRACT	18. NUMBER OF PAGES	19a. NAME OF RESPONSIBLE PERSON
a. REPORT	b. ABSTRACT	c. THIS PAGE			Joseph D Vasile
Unclassified	Unclassified	Unclassified	UU	35	19b. TELEPHONE NUMBER (Include area code) (410) 306-1794

Contents

List of Figures

List of Tables

Acknowledgments

The authors would like to thank Dr Jim DeSpirito, US Army Combat Capabilities Development Command (CCDC) Army Research Laboratory, for discussions regarding flow phenomena, aerodynamic fundamentals, and numerical techniques. Additionally, special thanks to Dr Ashish Nedungadi, The Johns Hopkins Applied Physics Laboratory, for his help and discussions regarding Cart3D fundamentals, techniques, and data-processing routines. This work was supported in part by a grant of high-performance computing time from the US Department of Defense (DOD) High Performance Computing Modernization program at the US Army CCDC Army Research Laboratory DOD Supercomputing Resource Center (DSRC), Aberdeen Proving Ground, Maryland, and the US Army Engineer Research and Development Center DSRC, Vicksburg, Mississippi.

1. Introduction

Most long-range projectiles are designed to be symmetric flight bodies, using low aspect ratio fins as control surfaces. During flight, these vehicles are typically roll stabilized at either the "+" (i.e., plus, $\phi = 0°$) or "x" (i.e., cross, $\phi = 45°$) orientation. At moderate to high angles of attack, the static forces and moments between these orientations can vary substantially.[1–8] This behavior could prove problematic when the flight controller executes a roll command for a projectile that is statically stable in one orientation (e.g., $\phi = 0°$) while being unstable in another (e.g., $\phi = 45°$). Moreover, this problem can be exacerbated when using lower-fidelity aerodynamic data sources (e.g., inviscid flow solvers), which can have limited accuracy for certain flight conditions. The purpose of this report is to show the importance of using higher-fidelity flow solvers to accurately characterize the roll orientation–dependent aerodynamics of long-range projectiles, as well as provide flow phenomena insights using flow visualization.

2. Vehicle Description

The projectile flight body used in the current investigation was shaped through a series of optimization analyses that identified design candidates with low drag and high lift-to-drag ratios. More description on the optimization process and airframe can be found in Vasile et al.[9–11] The nose tip was modeled as a blunt nose defined by a bluntness radius that is 0.1 of the diameter (i.e., 0.1 cal.). The Von-Karman ogive nose shape was used, with the length of the ogive section defined to be 0.3 of the overall length (OAL) of the projectile. The center of gravity of the flight vehicle was defined to be 0.6 of the OAL of the projectile. The body section was modeled as a constant axisymmetric cylinder. Additionally, a 7° boattail was modeled beginning 0.5 cal. forward of the base. The projectile was designed to be sabot-launched from an 8-inch-diameter gun, with no deploying aerodynamic surfaces. This requirement constrains the optimization to limit the fin span to 8 inches tip-to-tip. A leading edge sweep angle of 83° was used. All control surfaces had a root thickness of 4 mm and tapered down to 2 mm at the tip. The optimized fin set design for a given body baseline configuration with a 105-mm diameter, 10-cal. length, and ogive length of 30% of the overall length of the projectile is summarized in Table 1 and illustrated in Fig. 1.

Table 1. Summary of airframe design

Vehicle configuration	Diameter (mm)	Length-to-diameter	Ogive length of OAL	No. of fins	Root fin chord (cal.)	Tip fin chord (cal.)	Fin span (cal.)
Tail–fin control	105	10	0.3	4	6	2.2	1.935

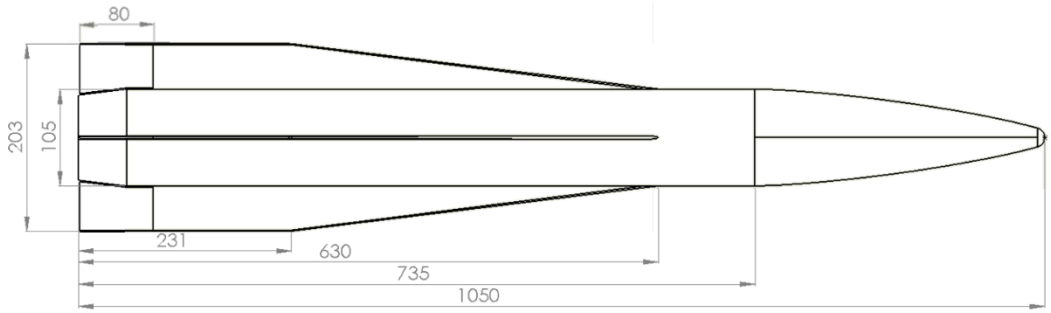

Fig. 1 Schematic of projectile flight body for a 105-mm diameter, length-to-diameter of 10, and ogive length of 30% of overall length. Dimensions are given in millimeters.

A full aerodynamic roll characterization of the vehicle was performed. The aerodynamic data for the entire airframe were simulated at multiple aerodynamic roll angles, spanning from 0° to 90°, every 22.5°. Figure 2 shows the projectile at four aerodynamic roll angles (i.e., ϕ = 0°, 22.5°, 45°, and 67.5°).

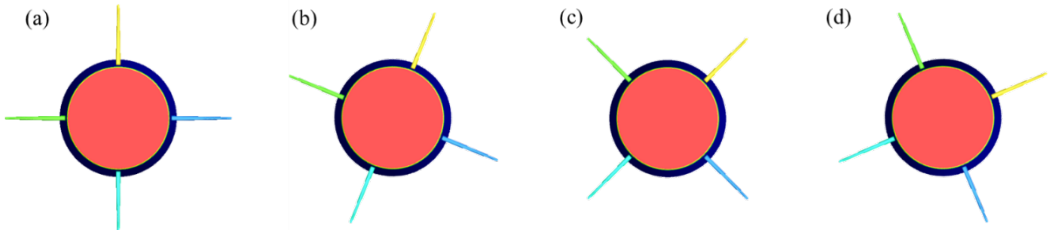

Fig. 2 Projectile flight body at aerodynamic roll angles ϕ = 0° (a), 22.5° (b), 45° (c), and 67.5° (d). View is from projectile base.

3. Computational Approach

Two aerodynamic data sources were used to characterize the projectile flight body. The aerodynamic sources used were an inviscid computational fluid dynamics (CFD) analysis package, NASA's Cart3D,[12] and a Navier–Stokes CFD flow solver, CFD++.[13]

3.1 Cart3D

NASA's Cart3D (1.5.5)[12] is an inviscid analysis package that allows for automated CFD analysis on complex aerodynamic designs. The Cartesian Euler CFD code was desirable since static aerodynamic coefficients for a given angle of attack could be computed in a matter of minutes. Cart3D quickly creates a Cartesian computational grid around the geometry after setting the domain's extent and resolution. The process uses adaptive mesh refinement (AMR) to increase fidelity of the meshed domain near small features and curvature of the geometry, thereby increasing the resolutions of the flow features present near the surface. The computational domain extended approximately 14 projectile lengths in all directions from the center of the projectile, and the smallest typical grid size for the domain was approximately 0.6 × 0.6 × 0.6 mm (Fig. 3). Mesh density regions were defined to refine the mesh near the surface as well as in the wake region to help resolve flow structures. These regions are further refined during the flow solution via the AMR. The computational domain consisted of approximately 6 million Cartesian cells. Once the mesh is generated, the flow solver (flowCart) exploits the features of the Cartesian grid to quickly compute the flow field and aerodynamic forces and moments experienced by the configuration. Since the Euler equations being solved do not include the viscous components, the Cart3D analysis package provides only inviscid aerodynamic coefficients. The static forces and moments were found for the entire vehicle across 17 Mach numbers (i.e., M_∞ = 0.45, 0.55, 0.65, 0.75, 0.85, 0.95, 1, 1.02, 1.2, 1.5, 2, 2.5, 3, 3.5, 4, 6, 9) at 16 angles of attack (i.e., $\alpha = 0°$ to 20°, every 2°, and $\alpha = 25°$ to 45°, every 5°), and at five aerodynamic roll angles (i.e., $\phi = 0°$ to 90°, every 22.5°).

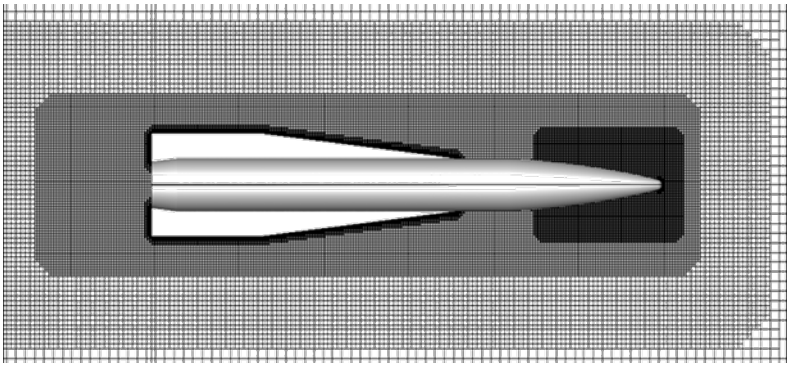

Fig. 3 Computational domain used for Cart3D

3.2 CFD++

The commercially available code CFD++ v18.1.1 by Metacomp Technologies, Inc.[13] was used for all Navier–Stokes CFD simulations. The 3-D compressible Reynolds-averaged Navier–Stokes equations were numerically solved to compute the flow solution. Steady-state and transient simulations were employed. The realizable k-ϵ two-equation turbulence model was used for all simulations.

The computational domain used was generated using the Capstone (version 9.1)[14] mesh generator. The total mesh size was approximately 43 M cells, consisting of triangular surface cells, with prism layers used along the surface and tetrahedral cells for the rest of the domain. The computational domain extended approximately 20 projectile lengths in all directions from the center of the projectile. The average cell size of the cylindrical density box (i.e., 2 cal. in radius, spanning 1 cal. forward to 5 cal. back of the projectile) was approximately 0.002 m. The first cell wall spacing of the prism layers was set to 3×10^{-7} m to ensure y^+ values of less than or equal to 1 along the surface of the projectile for all Mach numbers of interest. A close-up view of the near-field of the computational domain used for CFD++ simulations is presented in Fig. 4.

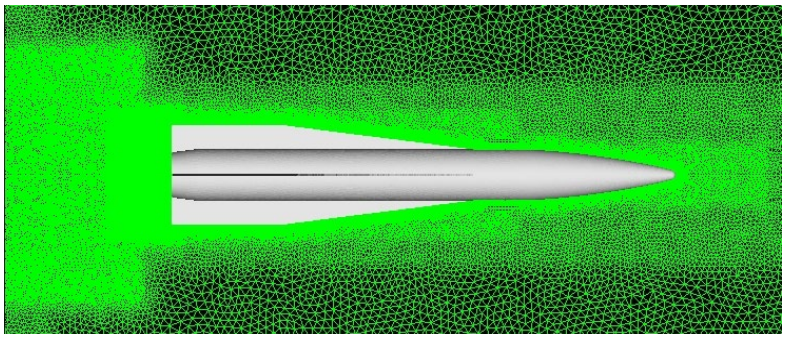

Fig. 4 Computational domain used for CFD++

Traditionally, aerodynamic information for projectiles has been obtained by computing the steady-state coefficients at multiple individual angles of attack. This method requires a lot of repetitive editing of input files, runs, and processing of computed results from these runs. A quasi-steady sweep procedure was instead employed; the procedure provides an easier method to consolidate the process and facilitates faster generation of aerodynamic data. More description on the quasi-steady sweep procedure can be found in Sahu and Fresconi.[15] The CFD data consist of static forces and moments of the entire vehicle without trailing-edge flap deflection across 18 Mach numbers (i.e., M_∞ = 0.7, 0.8, 0.9, 0.92, 0.94, 0.96, 0.98, 1.05, 1.1, 1.2, 1.5, 2, 2.5, 3, 3.5, 4, 4.5, 5) at four angles of attack (i.e., α = 0°, 2°, 5°, and 10°) and at five aerodynamic roll angles (i.e., ϕ = 0° to 90°, every 22.5°).

In addition to steady-state simulations, transient CFD simulations were performed to compute the pitch-dampening moment coefficients. A series of constrained pitch-oscillating simulations of the entire vehicle was performed. The pitch-oscillating simulations were performed at a single Mach number (i.e., $M_\infty = 2$), for three aerodynamic roll angles (i.e., $\phi = 0°$, 22.5°, and 45°). A nonlinear parameter estimation routine was applied to determine the pitch dampening moment coefficient for each vehicle orientation. This routine requires evolution equations that contain an aerodynamic model. More description on the parameter estimation routine can be found in Sahu and Fresconi.[16]

4. Results

4.1 Airframe Characterization

The static normal force and pitching moment coefficients computed for the entire vehicle computed at multiple angles of attack, across Mach number at two aerodynamic roll angles (i.e., $\phi = 0°$ and 45°), are presented in Figs. 5 and 6, respectively. The aerodynamic coefficients computed by Cart3D are presented as open triangle symbols, and the coefficients computed by CFD++ are presented by open circle symbols.

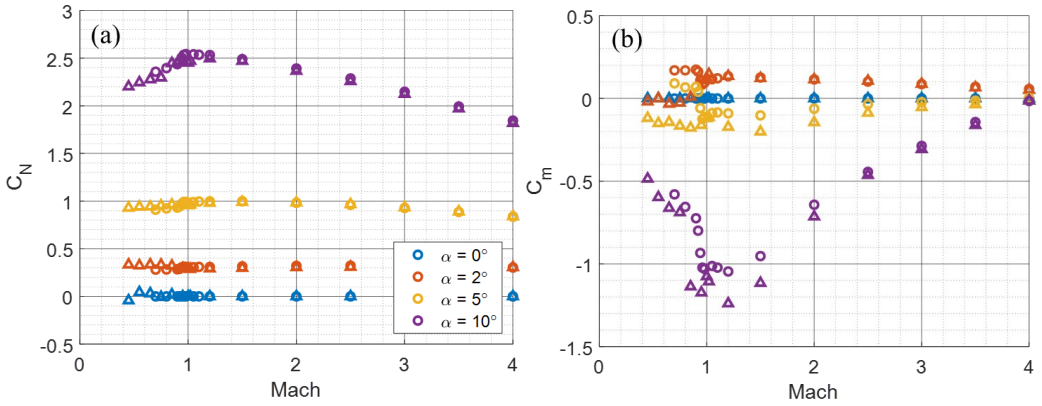

Fig. 5 Computed normal force (a) and pitching moment (b) coefficients of the entire vehicle, computed by Cart3D (open triangle symbols) and CFD++ (open circle symbols) at $\phi = 0°$

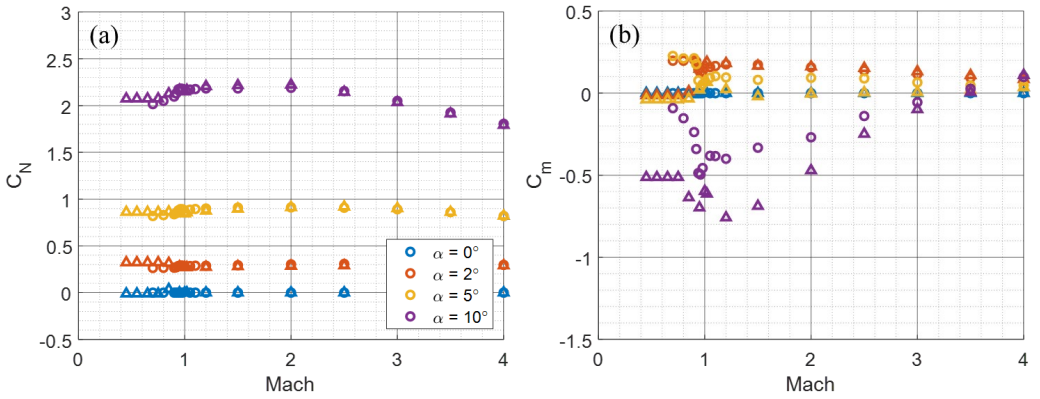

Fig. 6 Computed normal force (a) and pitching moment (b) coefficients of the entire vehicle, computed by Cart3D (open triangle symbols) and CFD++ (open circle symbols) at ϕ = 45°

In general, fins oriented in the "+" orientation produce more normal force as well as pitching moment coefficient magnitude. At ϕ = 45°, the normal force coefficient decreases approximately 10% compared to ϕ = 0°. As will be discussed in a later section, the addition of lifting surfaces exposed to the flow results in the generation of vortical structures that advect downstream near the body of the projectile. The results show that the projectile flight body is more statically stable in the "+" orientation (ϕ = 0°) than in the "x" orientation (ϕ = 45°). At ϕ = 45°, the pitching moment coefficient is approximately reduced by 40% compared to the ϕ = 0° orientation. This finding is important for projectile designers, as the static pitching moment coefficient is used to evaluate a vehicle's static stability. The design of the vehicle can dramatically change depending upon stability requirements, and therefore any proposed design for low-aspect-ratio finned projectiles requires a full aerodynamic roll characterization.

The computed aerodynamic coefficients between the CFD flow solvers compare reasonably well. The most noteworthy discovery is the large discrepancies of computed pitching moment coefficient between the CFD predictions at ϕ = 45°. The Cart3D results show a significant overprediction (approximately 40%) of the pitching moment coefficient magnitude compared to CFD++ at higher angles of attack across Mach number. The results suggest that viscous effects, specifically the viscous roll-up of vortical structures, play an important part in the computed pitching moment coefficient for low-aspect-ratio-finned projectiles. Further details and insights on the flow physics are presented in a later section. Although Cart3D is routinely used for the rapid development of high-speed projectiles and has been generally performed well compared to higher-fidelity CFD results, further caution must be taken at certain flight conditions where viscous effects could become relevant.

For the same flight conditions, the pitching moment coefficient is reduced when in the "x" orientation, indicating that there is a change in pressure distribution as well as center of pressure location of the entire vehicle. Figure 7 presents the computed center of pressure location of the entire vehicle at three angles of attack versus Mach number at two aerodynamic roll angles (i.e., $\phi = 0°$ and 45°).

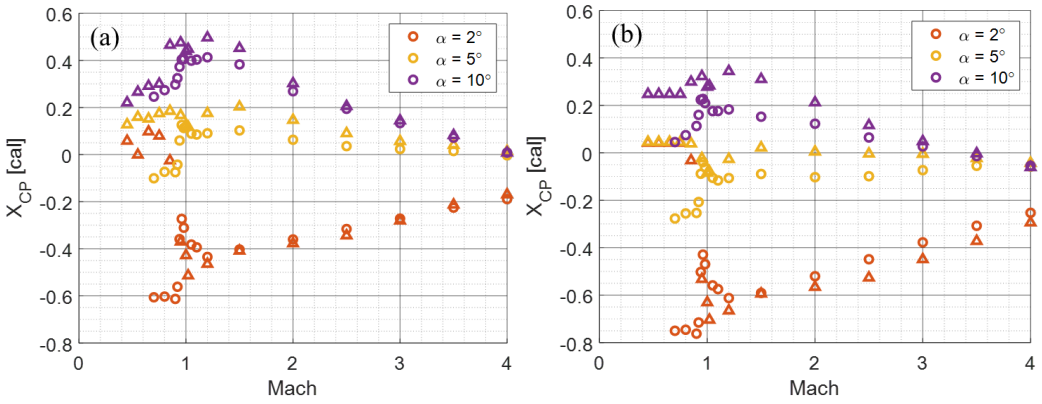

Fig. 7 Center of pressure location with respect to center of gravity computed by Cart3D (open triangle symbols), and CFD++ (open circle symbols) at $\phi = 0°$ (a) and $\phi = 45°$ (b)

As expected, at $\phi = 45°$, the reduction of X_{CP} indicates the center of pressure location shifts forward on the body, therefore reducing the stability of the vehicle. At this orientation, the leeward fins are in the wake of the body and at a lower Mach number compared to the windward fins. The exposed windward fins are more effective than the leeward fins, which causes the center of pressure to move forward. At $\phi = 0°$, the CFD flow solvers are in reasonable agreement, whereas at $\phi = 45°$, the results show discrepancies; Cart3D is unable to accurately predict the center of pressure location.

To better visualize the center of pressure relationship with aerodynamic roll angle, surface contours of pressure coefficient, C_P, of the projectile flight body were computed by CFD++. Figures 8 and 9 present the computed surface contours of pressure coefficient when viewed windward and leeward at three aerodynamic roll angles (i.e., $\phi = 0°$, 22.5°, and 45°) at $\alpha = 10°$, and $M_\infty = 2$, respectively. The surface pressure coefficient contour levels were set to be continuous between –0.2 to 0.2. As the projectile flight body rotates from the "+" orientation, $\phi = 0°$, to the "x" orientation, $\phi = 45°$, the surface pressure increases on the windward side of the projectile body. This region of higher pressure shifts forward (Fig. 8). The leeward surface pressure contours also provide insight to the influence of vortical flow structures generated at the fins, and therefore explain the observed reduction in normal force coefficient (Fig. 6). At $\phi = 22.5°$, the surface distribution is asymmetric between the fins, indicating that a side force is produced. As is

discussed, the surface pressure distribution is influenced by the vortical flow structures. At this aerodynamic roll angle, the vortical flow structures are asymmetric in size and strength, which results in an asymmetric pressure distribution on the vehicle.

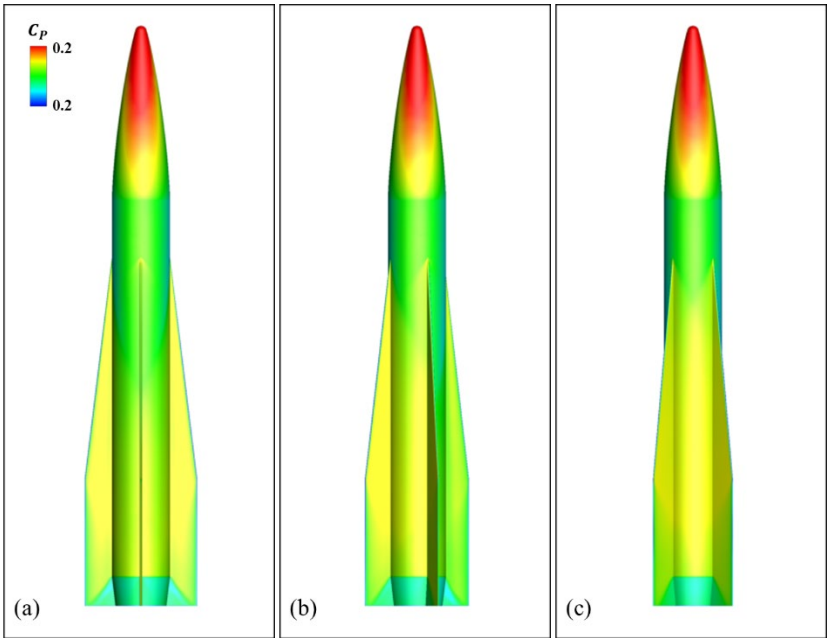

Fig. 8 Computed surface contours of pressure coefficient, C_P, of the windward side of projectile flight body at $\phi = 0°$ (a), 22.5° (b), and 45° (c) at $\alpha = 10°$ and $M_\infty = 2$

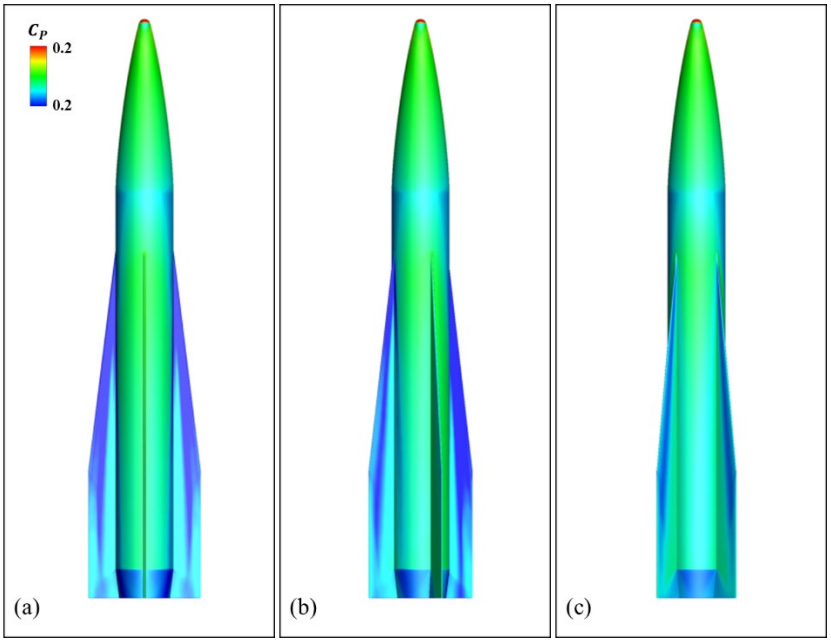

Fig. 9 Computed surface contours of pressure coefficient, C_P, of the leeward side of projectile flight body at $\phi = 0°$ (a), 22.5° (b), and 45° (c) at $\alpha = 10°$ and $M_\infty = 2$

To help quantify the effect of the aerodynamic roll orientation on the generation of the static forces and moments along the projectile body, a cumulative distribution that integrates the surface pressures in the axial direction along the length of the projectile was calculated. A total of 500 slices along the axial direction spaced equally from the nose to the base of the projectile were selected to integrate the surface pressures along the perimeter of the projectile. The resulting forces and moments along the projectile body at each axial location were computed and cumulatively summed.

The cumulative distribution of normal force coefficient along the projectile flight body from the forebody and fins components at $\phi = 0°$, 22.5°, and 45° at $\alpha = 10°$ and $M_\infty = 2$ is presented in Fig. 10a and 10b, respectively.

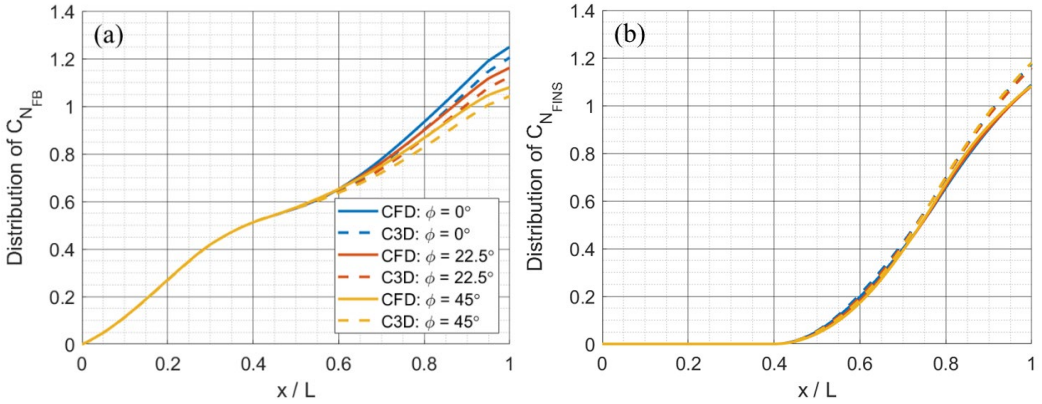

Fig. 10 Distribution of normal force coefficient along the projectile flight body from the forebody (a) and fins (b) components computed by Cart3D (dashed lines) and CFD++ (solid lines), at $\phi = 0°$, 22.5°, and 45° at $\alpha = 10°$ and $M_\infty = 2$

The results show that the normal force coefficient is produced along the projectile body and has an approximate equal contribution by both the forebody and fin components. For reference, the computed total normal force coefficients at $\phi = 0°$ and $\phi = 45°$ at these flight conditions are approximately 2.4 and 2.2, respectively (Figs. 5 and 6). Whereas the normal force is continually generated along the forebody beginning at the nose of the projectile, as expected, the fins begin to generate a normal force at the leading edge of the fins at the projectile body (i.e., x/L = 0.4). The production of normal force from the fins seems to be aerodynamic roll independent. The effect of aerodynamic roll orientation is primarily seen in the forebody. The results suggest that the flow structures that are generated by the fins interact and influence the surface pressures of the forebody. This is shown in Fig. 10a, where the largest difference between aerodynamic roll orientations is primarily found in the region where the fins are present. The results show that the major discrepancies between the numerical codes are present in the fin region of the vehicle. Compared to CFD++, the results from Cart3D predict less forebody

normal force and more fin normal force. The results indicate that there is a viscous flow effect near the vicinity of the surfaces of both forebody and fin components.

The cumulative distribution of side force coefficient along the projectile flight body from the forebody and fins components at ϕ = 0°, 22.5°, and 45° at α = 10° and M_∞ = 2 is presented in Fig. 11a and 11b, respectively.

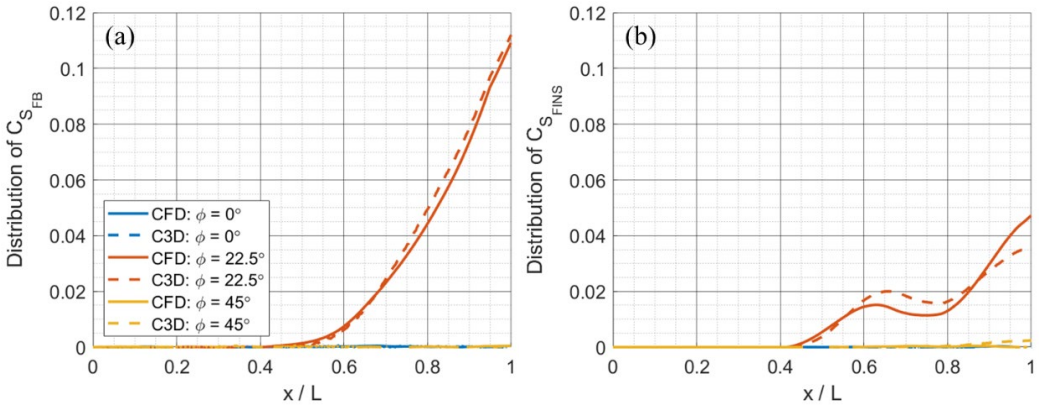

Fig. 11 Distribution of side force coefficient along the projectile flight body from the forebody (a) and fins (b) components computed by Cart3D (dashed lines) and CFD++ (solid lines), at ϕ = 0°, 22.5°, and 45° at α = 10° and M_∞ = 2

As expected, at both ϕ = 0° and 45°, due to symmetry, a negligible side force is generated along the projectile flight body. As was observed in Fig. 9, at ϕ = 22.5, there is an asymmetry in the surface pressure due to the generation of asymmetric vortical flow structures at the fins. The greatest contribution of the side force is generated by the forebody. The results confirm past experience that the asymmetric vortical flow structures induce flow near the surface of the forebody and cause the surface pressures to change, resulting in an asymmetric pressure distribution.[17] The results computed from Cart3D compare well to CFD++ for the forebody component. The major discrepancy is present in the fin component. The results suggest that vortical flow structures generated by the fins are not adequately modeled in Cart3D at ϕ = 22.5°.

The cumulative distribution of pitching moment coefficient along the projectile flight body from the forebody and fins components at ϕ = 0°, 22.5°, and 45° at α = 10° and M_∞ = 2 is presented in Fig. 12a and 12b, respectively.

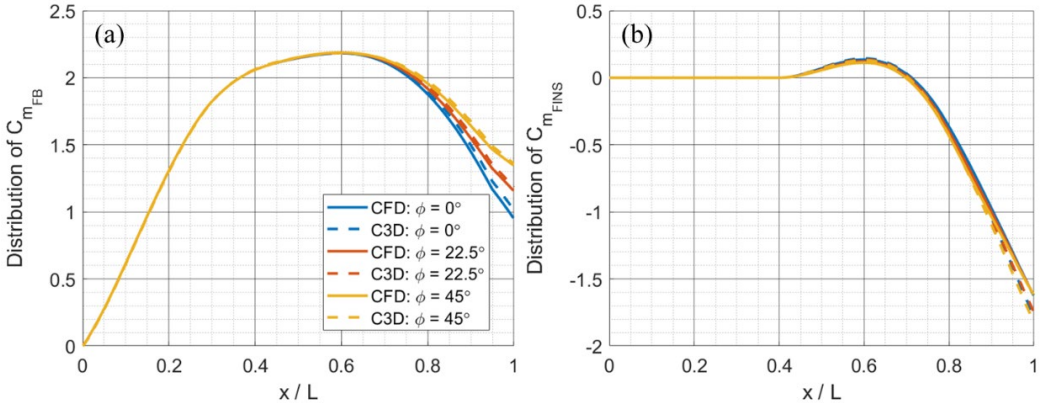

Fig. 12 Distribution of pitching moment coefficient along the projectile flight body from the forebody (a) and fins (b) components computed by Cart3D (dashed lines) and CFD++ (solid lines), at ϕ = 0°, 22.5°, and 45° at α = 10° and M_∞ = 2

The pitching moment coefficient distributions show the destabilizing contribution from the forebody and the stabilizing contribution from the fins. The center of gravity of the vehicle is located at 60% of the OAL, or x/L = 0.6. Therefore, the distribution of the pitching moment coefficient reaches a maximum at the center of gravity and then reduces aft of the center of gravity. As was found in Fig. 10, the fins are aerodynamic roll independent; however, the distributions of the forebody differ in the fin region. As similarly observed in the previous figures, the major discrepancies between Cart3D and CFD++ are present for the fin component. Cart3D overpredicts the pitching moment contribution from the fin components.

The cumulative distribution of yawing moment coefficient along the projectile flight body from the forebody and fins components at ϕ = 0°, 22.5°, and 45° at α = 10° and M_∞ = 2 is presented in Fig. 13a and 13b, respectively.

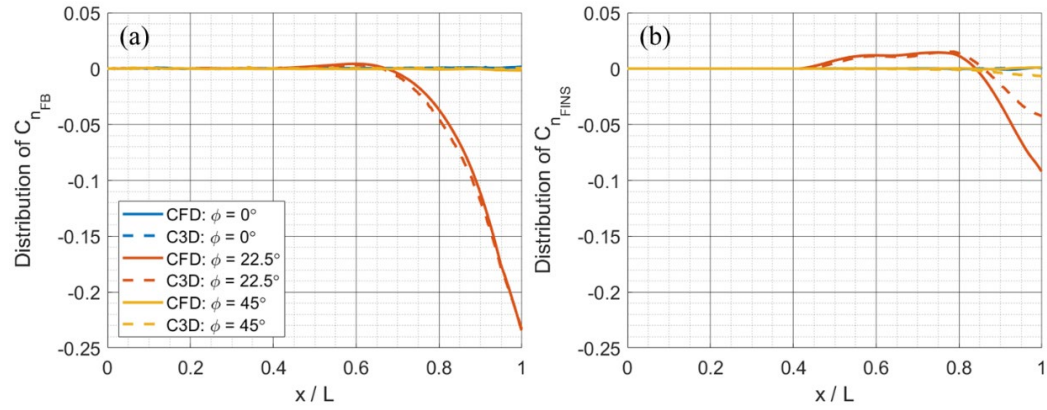

Fig. 13 Distribution of yawing moment coefficient along the projectile flight body from the forebody (a) and fins (b) components computed by Cart3D (dashed lines) and CFD++ (solid lines), at ϕ = 0°, 22.5°, and 45° at α = 10° and M_∞ = 2

As was similarly observed for the side force coefficient distribution, the projectile forebody is the major contributor to the yawing moment coefficient distribution for the $\phi = 22.5°$ configuration. The contribution from the fins initially produces a positive yawing moment, then switches to generating a negative yawing moment. This switching point coincides with the axial location where the fin switches from a swept fin to an unswept fin. The results suggest that the generation of the vortex at the leading edge of the fin versus at the tip affects the magnitude and direction of the yawing moment. As was observed in Fig. 11b, the discrepancy between Cart3D and CFD++ is evident in the fin component. The results indicate the discrepancy begins where the fin becomes unswept and increases along the axial direction.

To better visualize the discrepancies between Cart3D and CFD++ in the fin region, surface contours of pressure coefficient, C_P, on the projectile flight body were computed. A side view of the surface contours of pressure coefficient computed by Cart3D and CFD++ at $\phi = 45°$, $\alpha = 10°$, and $M_\infty = 2$ is presented in Fig. 14a and 14b, respectively. The surface pressure coefficient contour levels were set to be continuous between –0.01 to 0.01. A noted difference between the two predictions is observed primarily on the windward face of the leeward fin and the forebody near the fin–body junction. The results indicate that one or more vortical flow structures are present near the root of the leeward fins and influence the pressure distribution of the forebody and windward face of the leeward fin. These vortices, near the fin root, are predominantly a viscous effect, therefore Cart3D will never be able to resolve these small structures. The vortical flow structures increase the integrated pressure on the leeward side of the forebody and reduce the integrated pressure on the windward face of the leeward fin, with both effects resulting in a reduction of vehicle stability. Compared to Cart3D, CFD++ predicts higher integrated pressure on the forebody (stabilizing), but also a lower integrated pressure on the windward surface of the leeward fins. This latter effect dominates, resulting in lower predicted stability in CFD++ (see Fig. 12). Although not shown, the shock structure was similar between the two codes, therefore the observed differences in surface pressure distribution are attributed to the influence of the vortical flow structures. These vortical flow structures increase in size and magnitude as they advect downstream.

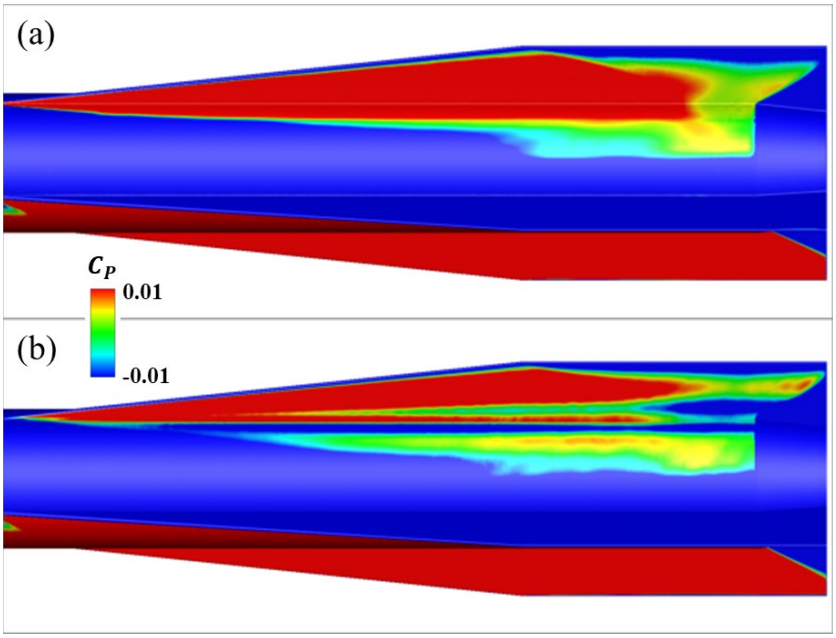

Fig. 14 Surface contours of pressure coefficient, C_P, computed by Cart3D (a) and CFD++ (b), viewed from the side of projectile flight body at $\phi = 45°$, at $\alpha = 10°$ and $M_\infty = 2$

The aerodynamic coefficients of the projectile flight body were calculated in the non-rolled aerodynamic body coordinate frame, with +X out the tail, +Y right, +Z up, as shown in Fig. 15a, and were converted to force and moments in the non-rolled standard flight dynamics body coordinate frame with +X out the nose, +Y right, +Z down, as shown in Fig. 15b. All coefficients in the following figures are in the latter flight dynamics body frame.

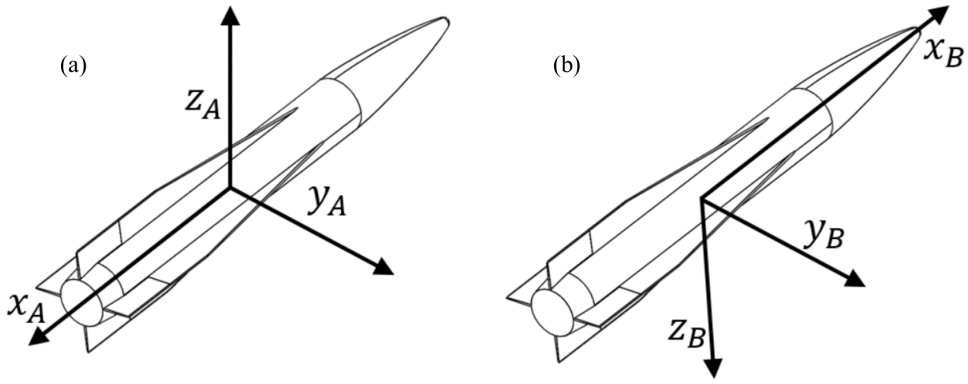

Fig. 15 Comparison of the non-rolled aerodynamic body coordinate frame (a) for the aerodynamic coefficients and the non-rolled flight dynamics body coordinate frame (b) for the calculated forces and moments

The total static forces and moments of the entire vehicle at two angles of attack ($\alpha = 4°$ and $10°$) at Mach 2 are presented in Fig. 16 versus aerodynamic roll angle. The aerodynamic roll distribution follows harmonic functions; the longitudinal (i.e., pitch) plane forces and moments are out-of-phase with respect to the lateral (i.e., yaw) plane forces and moments. The lateral forces and moments are at a maximum when the geometry of the projectile flight body is asymmetric to the incoming flow. In this position, the incoming flow impinges upon the fins, creating asymmetric vortical flow structures that cause an asymmetric pressure distribution, thus generating a side force and resulting moment.

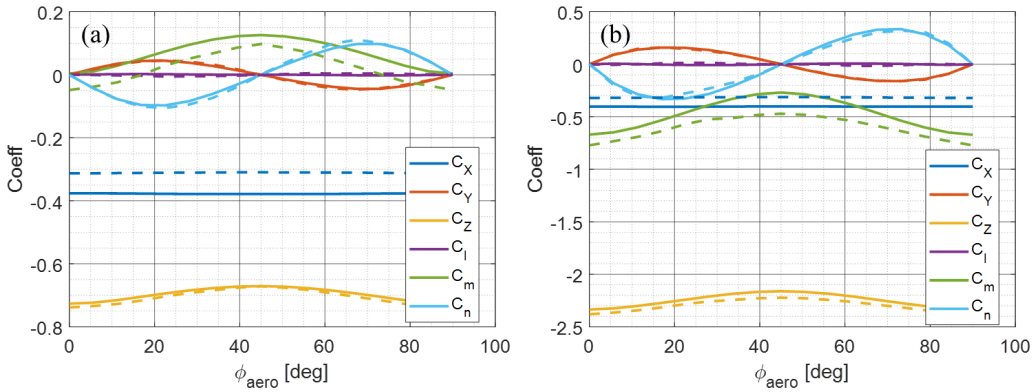

Fig. 16 Static aerodynamic coefficients of the projectile flight body at $\alpha = 4°$ (a) and $\alpha = 10°$ (b) computed by Cart3D (dashed lines) and CFD++ (solid lines) across aerodynamic roll angle, at $M_\infty = 2$

Since Cart3D is an inviscid flow solver, it was expected that the computed axial force was lower in magnitude than compared to CFD++. As was observed in Fig. 6, Cart3D overpredicts the magnitude of the pitching moment coefficient, predicting a more stable vehicle compared to CFD++. The computed normal force, side force, and yawing moment coefficient between the flow solvers compare remarkably well.

In addition to static aerodynamic coefficients, dynamic aerodynamic coefficients were computed from time-accurate CFD++ simulations. The pitch-dampening moment coefficient computed from constrained pitch-oscillating simulations of the flight vehicle at three aerodynamic roll angles (i.e., $\phi = 0°$, $22.5°$, and $45°$) and at Mach 2 is presented in Fig. 17. The results show that the magnitude of the pitch damping moment is significantly larger at $\phi = 45°$ than $\phi = 0°$.

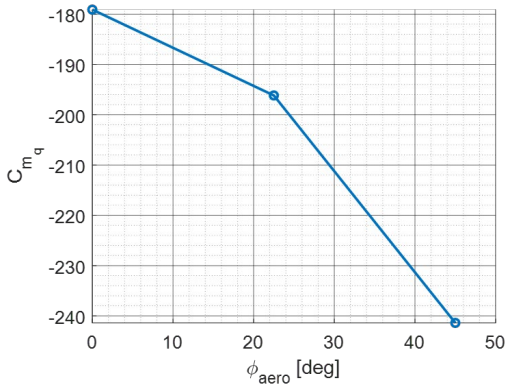

Fig. 17 Pitch dampening moment coefficient of projectile flight body computed by CFD++ at ϕ = 0°, 22.5°, and 45°, and at M_∞ = 2

4.2 Flow Visualization

The full aerodynamic roll characterization of the projectile flight body revealed that the aerodynamic coefficients are aerodynamic roll angle dependent when the projectile is at an appreciable angle of attack. Furthermore, it was found that the static normal force reduced in magnitude, and the static longitudinal stability reached a minimum at ϕ = 45°. At this aerodynamic roll angle, Cart3D predicted an overall more stable vehicle compared to the higher-fidelity results from CFD++. The results suggest that there are viscous flow phenomena that become significant when the lifting fins are in an asymmetric orientation such that both windward and leeward fins are subject to the crossflow. To improve our understanding of the flow physics associated with long-range projectiles, the generation and advection of the vortical structures produced by the fins were studied.

Qualitative plots of scaled Q-criterion iso-surfaces superimposed with contours of pressure coefficient on the surface of the flight body projectile at α = 4° and 10°, and M_∞ = 2, computed from Cart3D (a, c, e, g) and CFD++ (b, d, f, h), at ϕ = 0° (a, b), 22.5° (c, d), 45° (e, f) and 67.5° (g, h), are presented in Figs. 18 and 19, respectively. The Q-criterion was developed to help isolate the vortex features from the vorticity present in the boundary layer by defining vortices in flows as spatial regions where the vorticity tensor dominates the rate of strain.[18] The scaled Q-criterion, Q_S, is mathematically expressed in Eq. 1:

$$Q_S = \frac{1}{2}\left(\frac{\|\Omega\|^2}{\|S\|^2} - 1\right) \tag{1}$$

where $\boldsymbol{\Omega}$ and $\boldsymbol{S}$ are the vorticity tensor and rate of strain tensor, respectively. The scaled Q-criterion iso-surfaces allow for visual observation of the vortical structures that are formed at the tip of the fins. The iso-surface value was set to 1.5. The iso-surface was colored based on the magnitude of streamwise vorticity at the same location. The surface pressure coefficient contour levels were set to be continuous between –0.2 to 0.2.

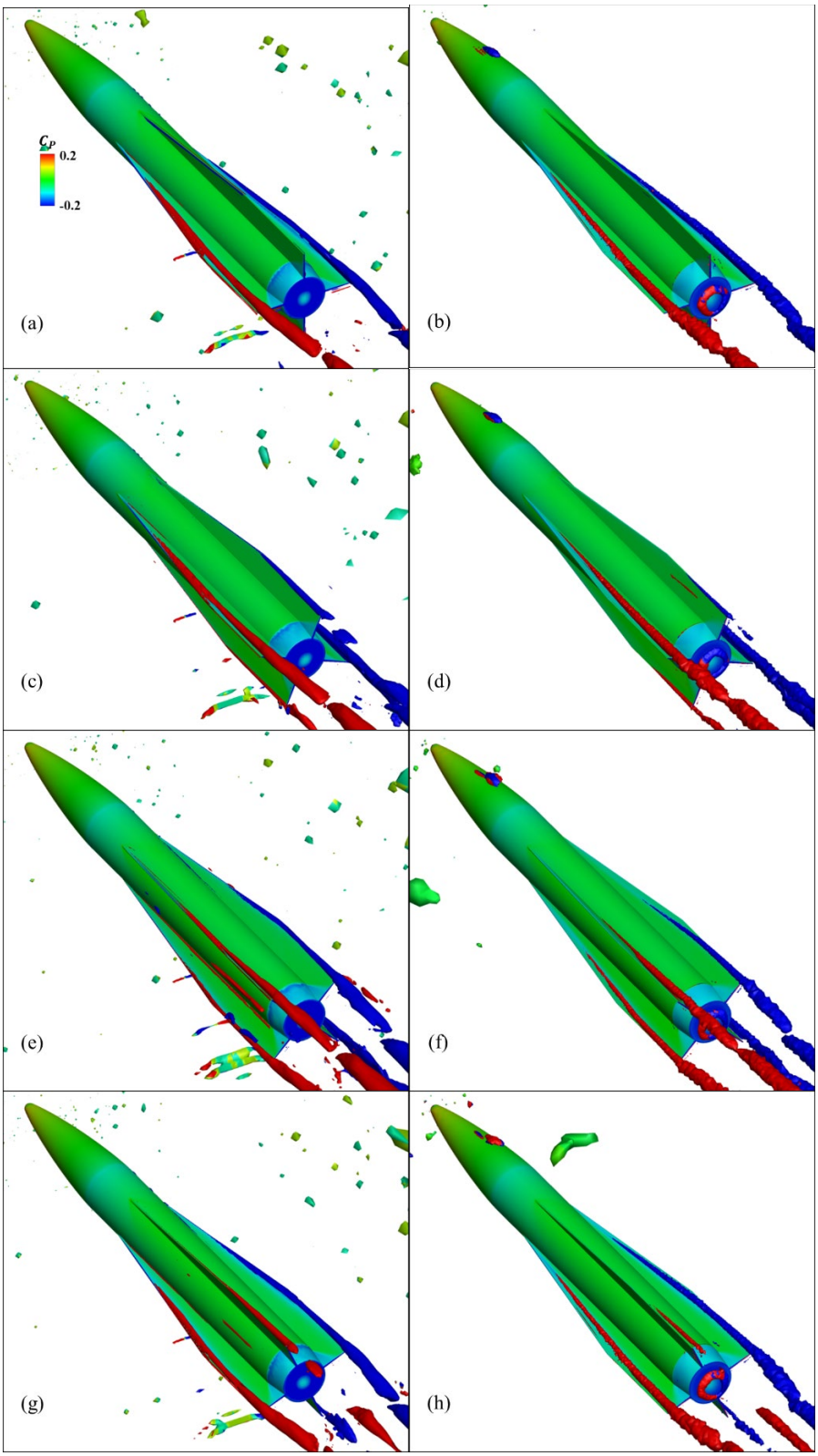

Fig. 18 Surface contours of pressure coefficient superimposed with iso-surfaces of scaled Q-criterion (Q_S = 1.5) colored by streamwise vorticity at ϕ = 0° (a-b), ϕ = 22.5° (c-d), ϕ = 45° (e-f), and ϕ = 67.5° (g-h), computed by Cart3D (a, c, e, g) and CFD++ (b, d, f, h) at α = 4° and M_∞ = 2

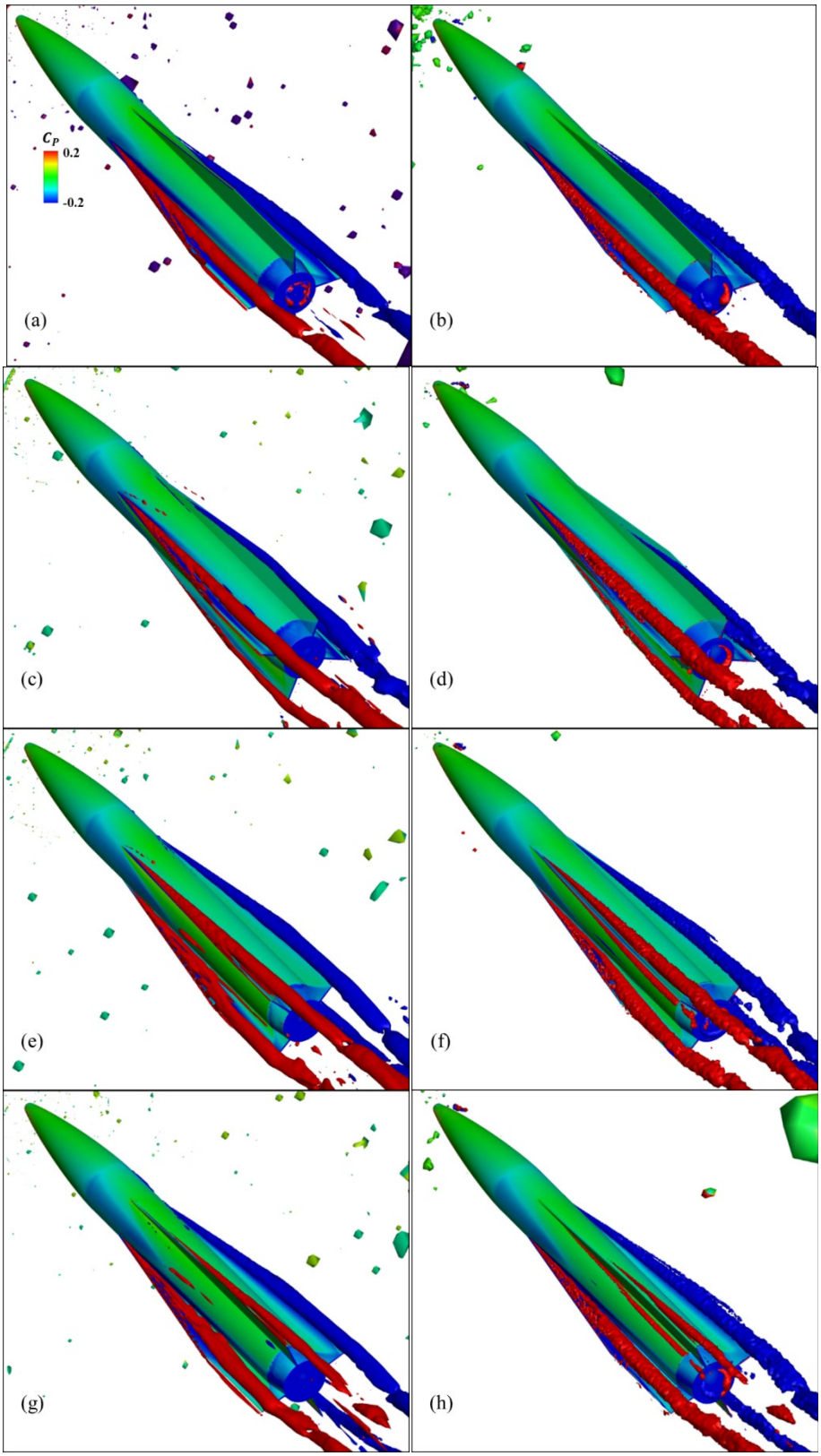

Fig. 19 Surface contours of pressure coefficient superimposed with iso-surfaces of scaled Q-criterion (Q_S = 1.5) colored by streamwise vorticity at ϕ = 0° (a-b), ϕ = 22.5° (c-d), ϕ = 45° (e-f), and ϕ = 67.5° (g-h), computed by Cart3D (a, c, e, g) and CFD++ (b, d, f, h) at α = 10° and M_∞ = 2

For all aerodynamic roll angles, vortical flow structures are generated along the leading edge of the swept portion the fin. Increasing the angle of attack results in an increase in size and strength of the vortical structures. At $\phi = 0°$, two large vortical structures are generated along the fins, which are perpendicular to the incoming flow. These flow structures advect downstream, increasing in size and magnitude. The vortical structures remain close to the fin and body, causing a reduction in pressure on the surfaces near the flow structure. This reduction of pressure increases the pressure difference across the projectile body, therefore increasing the lift of the vehicle. Rotating the projectile flight body to $\phi = 22.5°$ causes the generation of additional vortical structures on the additional lifting fins exposed to the flow. However, due to the orientation of the fins, vortical structures are asymmetric in size and strength, therefore explaining the generation of a side force and yawing moment as observed in Fig. 16. At $\phi = 45°$, all four fins are generating vortical flow structures, and these structures are symmetric in size and magnitude. Due to the presence of additional flow structures, the surface pressure distribution changes, therefore explaining the change in center of pressure location (Fig. 7).

The computed vortical flow structures predicted by Cart3D and CFD++ are in relatively good agreement. There are some discrepancies as the aerodynamic roll angle increases. This is natural, since the inviscid code does not include the viscous roll-up as the vortex is formed along the fin tip. This effect can be observed in Fig. 18, where the roll-up in the Cart3D solutions begins at the fin tip, while the roll-up in the viscous CFD++ solutions is delayed and occurs slightly inboard of the tip. At the higher angle of attack, Fig. 19, the viscous roll-up effect is reduced, and leading-edge vortices occur at similar locations in both simulations. As the body roll angle is increased, at the higher angle of attack (Fig. 19), additional differences in the vortex structures exist between the inviscid and viscous CFD solutions. A primary difference is the presence of a vortex structure near the root of the windward side of the leeward fin. This is the structure responsible for the surface pressure differences shown in Fig. 14.

To better visualize the generation and advection of these vortical structures, contour slices of normalized total pressure superimposed with contours of pressure coefficient on the surface of the flight body projectile, at $\alpha = 4°$ and 10°, and $M_\infty = 2$, computed from Cart3D (a, c, e, g) and CFD++ (b, d, f, h), at $\phi = 0°$ (a, b), 22.5° (c, d), 45° (e, f) and 67.5° (g, h), are presented in Figs. 20 and 21, respectively. A total of 10 contour slices, equally spaced 1 cal., starting from 1 cal. downstream of the projectile nose to 2 cal. aft of the projectile base were used. Although Cart3D is able to predict large vortical flow structures that are similar to CFD++, the inviscid flow solver is unable to resolve the viscous roll-up the vortical structures

that are evident in the CFD++ results. This difference in the vortex structure causes differences in the intensity of the vortices on the leeward side of the leeward fins. Moreover, at $\phi = 45°$, Cart3D is unable to resolve the vortical flow structure along the root on the windward face of the leeward fins. These root vortices are predominantly a viscous effect; therefore, Cart3D will never be able to resolve these small structures. These relatively small discrepancies in the structure and location of vortices ultimately result in noticeable discrepancies in the computed aerodynamic coefficients of the projectile (see Figs. 5–7).

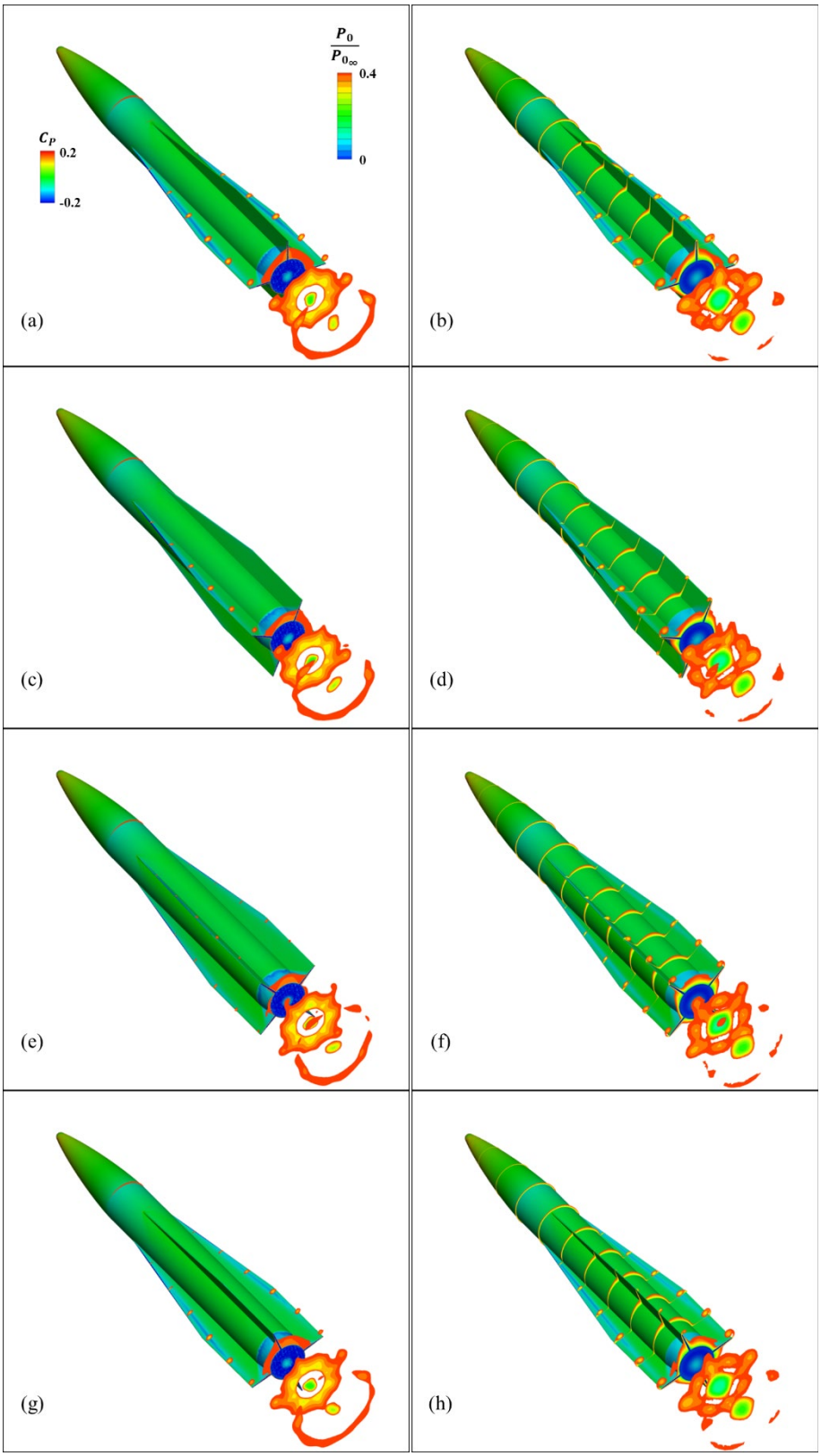

Fig. 20 Surface contours of pressure coefficient superimposed with contour slices of normalized total pressure at ϕ = 0° (a, b), ϕ = 22.5° (c, d), ϕ = 45° (e, f), and ϕ = 67.5° (g, h) computed by Cart3D (a, c, e, g) and CFD++ (b, d, f, h) at α = 4° and M_∞ = 2

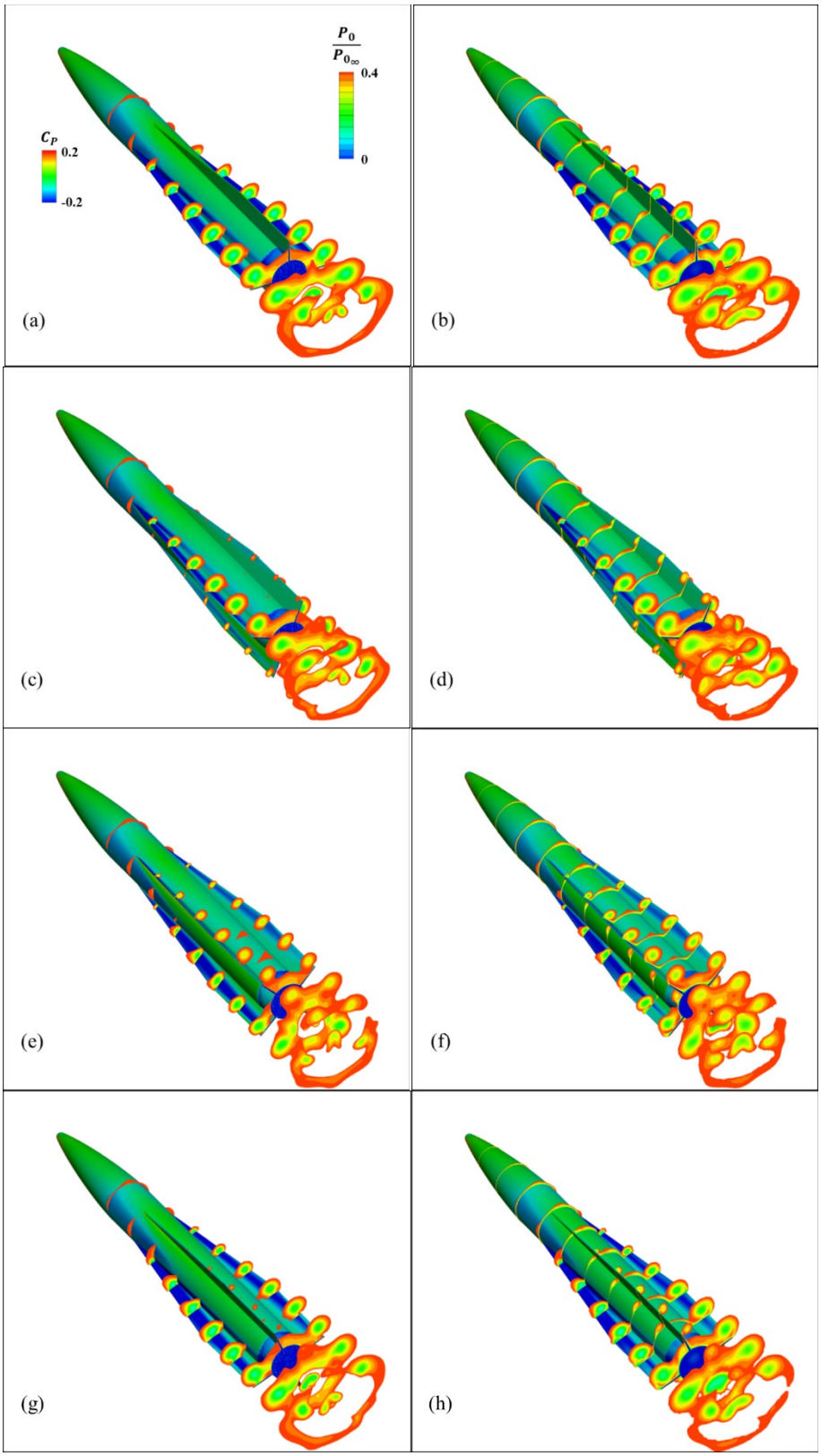

Fig. 21 Surface contours of pressure coefficient superimposed with contour slices of normalized total pressure at $\phi = 0°$ (a, b), $\phi = 22.5°$ (c, d), $\phi = 45°$ (e, f), and $\phi = 67.5°$ (g, h) computed by Cart3D (a, c, e, g) and CFD++ (b, d, f, h) at $\alpha = 10°$ and $M_\infty = 2$

5. Conclusion and Future Work

A comprehensive effort was undertaken to aerodynamically characterize a low-aspect-ratio finned projectile across Mach, angle of attack, and aerodynamic roll angle. The CFD flow solvers Cart3D and CFD++ were used to compute and compare the aerodynamic coefficients of the vehicle. In general, Cart3D compared reasonably well for all static aerodynamic coefficients except for pitching moment coefficient. The results showed that modeling viscous effects is necessary to accurately predict the pitching moment coefficient. Since Cart3D is an inviscid flow solver, it is unable to resolve the viscous roll up of the vortical structures generated along the fin, therefore inaccurately predicting the center of pressure location and leading to incorrect stability predictions for some vehicle orientations. Future work planned, including both spark range and wind tunnel experiments, will provide supporting validation data for these predictions.

6. References

1. Pepitone TR. The influence of roll orientation-dependent aerodynamics on the stability of cruciform missile configurations. Dahlgren (VA): Naval Surface Weapons Center; 1981. Report No.: NSWC-TR-79-416.

2. Pepitone TR, Jacobson ID. Resonant behavior of a symmetric missile having roll orientation-dependent aerodynamics. Journal of Guidance, Control, and Dynamics. 1978;1(5):335–339.

3. Nielsen JN, Hemsch MJ, Smith CA. A preliminary method for calculating the aerodynamic characteristics of cruciform missiles to high angles of attack including effects of roll angle and control deflections. Mountain View (CA): Nielsen Engineering and Research Inc.; 1977. Report No.: ONR-CR215-226-4F.

4. Moore FG, McInville RM. Nonlinear aeroprediction methodology for roll positions of 45 degrees. Journal of Spacecraft and Rockets. 1997;34(1):54–61.

5. Oberkampf WL. Prediction of forces and moments on finned missiles at high angle of attack in transonic flow. Eglin Air Force Base (FL): Air Force Armament Laboratory; 1980. Report No.: AFATL-TR-80-107.

6. Reece EW. Six component force test of the TX-61 at Mach 0.7 to 2.5 with varying angles of attack and roll angles. Albuquerque (NM): Sandia National Laboratories; 1966. Report No.: SC-JM-65-575.

7. Reece EW. Results of a wind tunnel test to determine the effect of roll position on the longitudinal static stability of the tomahawk rocket configuration at Mach 7.3. Albuquerque (NM): Sandia National Laboratories; 1966. Report No.: SC-TM-66-495.

8. Regan FJ, Shermerhorn VL, Falusi ME. Roll-induced force and moment measurements of the M823 research store. White Oak (MD): Naval Ordnance Laboratory (US); 1968. Report No.: NOLTR 68-195.

9. Vasile J, Bryson J, Fresconi F. Aerodynamic design optimization of long range projectiles using missile DATCOM. Aberdeen Proving Ground (MD): CCDC Army Research Laboratory; 2020. Report No.: ARL-TR-8936.

10. Vasile J, Bryson J, Fresconi F. Aerodynamic design optimization of long range projectiles using missile DATCOM. AIAA Scitech 2020 Forum; 2020; Orlando, FL. AIAA Paper 2020–1762.

11. Vasile J, Bryson J, Sahu J, Paul J, Gruenwald B. Aerodynamic dataset generation of a long range projectile. Aberdeen Proving Ground (MD): CCDC Army Research Laboratory; in press.

12. Aftosmis MJ, Berger MJ, Adomavicius G. A parallel multilevel method for adaptively refined Cartesian grids with embedded boundaries. 38th Aerospace Sciences Meeting and Exhibit; 2000; Reno, NV. AIAA Paper 2000-0808.

13. Metacomp Technologies, Inc. CFD++ user manual. Agoura Hills (CA): Metacomp Technologies, Inc.; 2018.

14. Dey S, Aubry RM, Karamete BK, Mestreau EL. Capstone: a geometry-centric platform to enable physics-based simulation and system design. Comput Sci Eng. 2016;18(1):32–39.

15. Sahu J, Fresconi F. Fast generation of aerodynamics data for a canard-controlled body with thrust-vector control. AIAA Aviation 2019 Forum; 2019; Dallas, TX. AIAA Paper 2019-3163.

16. Sahu J, Fresconi F. Flight behaviors of a complex projectile using a coupled CFD-based simulation technique: free motion. AIAA Aviation 2015 Forum; 2015; Dallas, TX. AIAA Paper 2015-2585.

17. Mahadevan S, Rodriguez J, Kumar R. Effect of controlled imperfections on the vortex asymmetry of a conical body. AIAA J. 2018;56(9):3460–3477.

18. Hunt JCR, Wray AA, Moin P. Eddies, streams, and convergence zones in turbulent flows. Stanford (CA): Stanford University, Center for Turbulence; 1988. p. 193. Research Report No.: CTR-S88.

List of Symbols, Abbreviations, and Acronyms

AMR	adaptive mesh refinement
CCDC	US Army Combat Capabilities Development Command
CFD	computational fluid dynamics
DOD	Department of Defense
DSRC	DOD Supercomputing Resource Center
NASA	National Aeronautics and Space Administration
OAL	overall length

Nomenclature

ϕ	=	aerodynamic roll angle
M_∞	=	freestream Mach number
α	=	angle of attack
C_N	=	normal force coefficient
C_m	=	pitching moment coefficient
X_{CP}	=	center of pressure location with respect to center of gravity
C_{m_q}	=	pitch damping coefficient sum (i.e., $C_{m_q} + C_{m_{\dot{\alpha}}}$)
Q_S	=	scaled Q-criterion
$\boldsymbol{\Omega}$	=	vorticity tensor
$\boldsymbol{S}$	=	strain tensor
C_P	=	pressure coefficient
C_X	=	non-rolled x-axis force coefficient
C_Y	=	non-rolled y-axis force coefficient
C_Z	=	non-rolled z-axis force coefficient
C_l	=	rolling moment coefficient
C_n	=	yawing moment coefficient
P_0	=	total pressure
P_{0_∞}	=	freestream total pressure

1 (PDF) DEFENSE TECHNICAL INFORMATION CTR DTIC OCA

1 (PDF) CCDC ARL
FCDD RLD CL
TECH LIB

1 (PDF) CCDC AC
RDAR MEM A
M DUCA

3 (PDF) CCDC AVMC
FCDD AMS MMA
J DOYLE
C ROSEMA
M MCDANIEL

1 (PDF) JHU/APL
A NEDUNGADI

28 (PDF) CCDC ARL
FCDD RLW
J ZABINSKI
FCDD RLW A
F FRESCONI III
FCDD RLW L
W OBERLE
P PEREGINO
T SHEPPARD
FCDD RLW LB
N TRIVEDI
E BYRD
FCDD RLW LC
J SADLER
FCDD RLW LD
A WILLIAMS
M NUSCA
A MCBAIN
FCDD RLW LH
M MINNICINO
R SUMMERS
FCDD RLW ME
S SILTON
FCDD RLW LE
J VASILE
J BRYSON
J DESPIRITO
L STROHM
J PAUL
V BHAGWANDIN
L FAIRFAX
B GRUENWALD
I CELMINS
J SAHU
FCDD RLW LF
M ILG
B TOPPER
D EVERSON
T BROWN